Article

The Essential Role of Monte Carlo Simulations for Lung Dosimetry in Liver Radioembolization with ^{90}Y Microspheres

Edoardo d'Andrea [1,2], Nico Lanconelli [3], Marta Cremonesi [4], Vincenzo Patera [5,6] and Massimiliano Pacilio [2,*]

1 Postgraduate School of Medical Physics, Azienda Ospedaliero-Universitaria Policlinico Umberto I, 00161 Rome, Italy; dandrea.phys@gmail.com
2 Department of Medical Physics, Azienda Ospedaliero-Universitaria Policlinico Umberto I, 00161 Rome, Italy
3 Department of Physics and Astronomy, Università di Bologna, 40126 Bologna, Italy; nico.lanconelli@unibo.it
4 Medical Physics Unit, IEO, European Institute of Oncology IRCCS, 20141 Milan, Italy; marta.cremonesi@ieo.it
5 Department of Basic and Applied Science for Engineering, University of Roma "Sapienza", 00161 Rome, Italy; vincenzo.patera@uniroma1.it
6 Sezione di Roma I, Istituto Nazionale di Fisica Nucleare, 00161 Rome, Italy
* Correspondence: m.pacilio@policlinicoumberto1.it

Abstract: This study compares various methodologies for lung dosimetry in radioembolization using Monte Carlo (MC) simulations. A voxelized anthropomorphic phantom, created from a real patient's CT scan, preserved the actual density distribution of the lungs. Lung dosimetry was evaluated for five lung-shunt (LS) cases using traditional methods: the mono-compartmental organ-level approach (MIRD), local energy deposition (LED), and convolution with voxel S-values, either with local density corrections (SVOX_L) or without (SVOX_ST). Additionally, a novel voxel S-value (VSV) kernel for lung tissue with an ICRU density of 0.296 g/cm^3 was developed. Calculations were performed using either the ICRU lung density (Lung_296), the average lung density of the phantom (Lung_221), or the local density (Lung_L). The comparison revealed significant underestimations in the mean absorbed dose (AD) for the classical approaches: approximately −40% for MIRD, −27% for LED, −28% for SVOX_L, and −88% for SVOX_ST. Similarly, calculations with the lung VSV kernel showed underestimations of about −62% for Lung_296, −50% for Lung_221, and −35% for Lung_L. Given the high heterogeneity of lung tissue, traditional dosimetric methods fail to provide accurate estimates of the mean *AD* for the lungs. Therefore, *MC* dosimetry based on patient images is recommended as the preferred method for precise assessment of lung *AD* during radioembolization.

Keywords: lung shunt; internal dosimetry; Monte Carlo; radioembolization; Y90; sirt; tare; lung dosimetry

1. Introduction

Liver cancer is the sixth most commonly diagnosed cancer and the third leading cause of cancer-related death worldwide [1]. Trans-arterial radioembolization (TARE) via intrahepatic administration of Yttrium-90 (^{90}Y-loaded microspheres (MS)) is a minimally invasive therapy that has been used for many years for the treatment of hepatocellular carcinoma (HCC) and liver metastases from other malignancies.

^{90}Y is a nearly pure β^- emitter with an average energy of 0.927 MeV and a half-life of 2.67 days. Over 99% of the time, ^{90}Y decays via β^- emission to the ground state of zirconium-90 (^{90}Zr). A small fraction of the radionuclide (about 0.01%) decays to the excited 0$^+$ state of ^{90}Zr, which subsequently decays to the ground state via internal conversion, internal pair production, or two-photon de-excitation [2,3]. The maximum range of β^- radiation in soft tissue, based on the continuous slowing down approximation (CSDA), is about 11 mm [2,3]. This radiation causes damage to tumor cells via cytotoxic effects induced by radiolytically generated reactive species. The administration of ^{90}Y-labeled microspheres is preceded by appropriate embolization of the vascular bed performed by the

interventional radiologist to optimize the targeting and deposition of radioactivity in the tumor while sparing as much hepatic parenchyma as possible and minimizing pulmonary and gastrointestinal shunting.

The most common devices are resin MS (SIR-Spheres®, Sirtex Medical Limited Australia, Sydney, Australia) [4] and glass MS (TheraSphere®, Boston Scientific Corporation, Marlborough, MA, USA) [5]. Radioembolization (RE) is preceded by diagnostic liver angiography, combined with an intra-arterial injection of ^{99m}Tc-macroaggregated albumin (MAA) at the treatment site, followed by scintigraphic imaging. This process is used to perform arterial mapping, identify patients with contraindications to treatment, and target the tumors.

The prescribed absorbed dose to tumor lesions varies depending on the patient-specific scenario and the microsphere device. It is typically around 100–120 Gy for glass microspheres and over 180 Gy for resin microspheres [4–8]. The main contraindications are the presence of gastrointestinal shunting and lung shunting, which result in an absorbed dose to the lungs of more than 30 Gy [2,3].

The use of TARE as a neoadjuvant approach to hepatic lobectomy [9] or as a bridge to transplantation [10] is gaining interest in the clinical landscape of liver diseases. Personalized dosimetry is essential for effective patient management and achieving clinical goals. In this context, the ability to increase the administered activity is both highly desirable and attainable, provided that appropriate treatment planning, especially for estimating the absorbed dose to the lungs in the presence of a lung shunt, has been carried out. The state of the art in lung dosimetry is based on the recommendations of the American Association of Physicists in Medicine (AAPM) [2], the European Association of Nuclear Medicine (EANM) [3], and the manufacturers [4,5]. In some cases, estimating the absorbed dose is impossible due to a lack of morphologic data, such as abdominal computed tomography (CT) scans that are truncated at the lungs or when there is no available morphological examination of the lung tissue. Under such conditions, the only option to assess the tolerability of the treatment is to compute the lung shunt fraction. This fraction must conventionally be lower than 20%, assuming a lung mass of 1 kg and an upper absorbed dose limit of 30 Gy [2,3]. The absence of proper methodology for lung dosimetry could lead to cases of radiation-induced pneumonitis, even in unexpected lung shunting scenarios or when blindly following the manufacturer's instructions [11]. This highlights the need to establish a lung-specific dosimetry workflow.

In tissues with densities similar to soft tissue and with unmarked tissue heterogeneities, approximate calculation methodologies have achieved excellent results, even when compared to Monte Carlo (MC) simulations on patients [12–15]. In contexts where tissue heterogeneities are significant, especially with low-density tissues, the physical conditions of radiation transport make the applicability of methods other than direct *MC* simulations questionable, necessitating further evaluation. In clinical contexts beyond RE, such as the treatment of iodine-avid metastases from differentiated thyroid carcinoma or Hodgkin's lymphoma in the lung with radioiodine [16,17], the fundamental role of accurate *MC* simulation in internal dosimetry and its impact on treatment success have been evaluated. This suggests that a similar evaluation may be necessary for dosimetry in RE, particularly in cases with significant pulmonary shunts.

This study aims to evaluate the most commonly used dosimetric approaches in RE for estimating the absorbed dose to the lungs. This evaluation will be conducted using an anthropomorphic CT-derived voxelized phantom with various lung shunt fraction cases, and the results will be compared with *MC* simulations of direct radiation transport.

2. Materials and Methods

2.1. Anthropomorphic Voxelized Phantom

A voxelized anthropomorphic phantom, based on the CT scan (voxel size of 1.37 × 1.37 × 3.27 mm^3) of a healthy male patient, weighing 72 kg and 166 cm tall, was created using ITK-Snap software (version 3.8.0) [18]. The phantom was then resampled to a cubic

voxel grid with a voxel size of 2.21 mm using the "Resample Scalar Volume" built-in module of 3D-Slicer software (version 5.2.2) [19], applying the "nearest neighbor" algorithm [20]. Three spherical lesions were artificially introduced into the phantom's liver, with diameters of 10, 20, and 30 mm. These lesions had a higher density than the liver parenchyma, i.e., 1.20 g/cm^3 for tumor tissue, compared to 1.04 g/cm^3 assigned to the surrounding tissue [21,22]. For the lung tissue, the actual spatial density distribution of the patient was assumed for this phantom, based on the HU-density calibration of the CT scanner. The phantom's lung density distribution ranges from 0 to 1.06 g/cm^3, with a mean value of 0.221 g/cm^3 and a median of 0.179 g/cm^3. A visual representation is provided in Figure 1, which displays a histogram of the voxel density values within the lung Region of Interest (ROI).
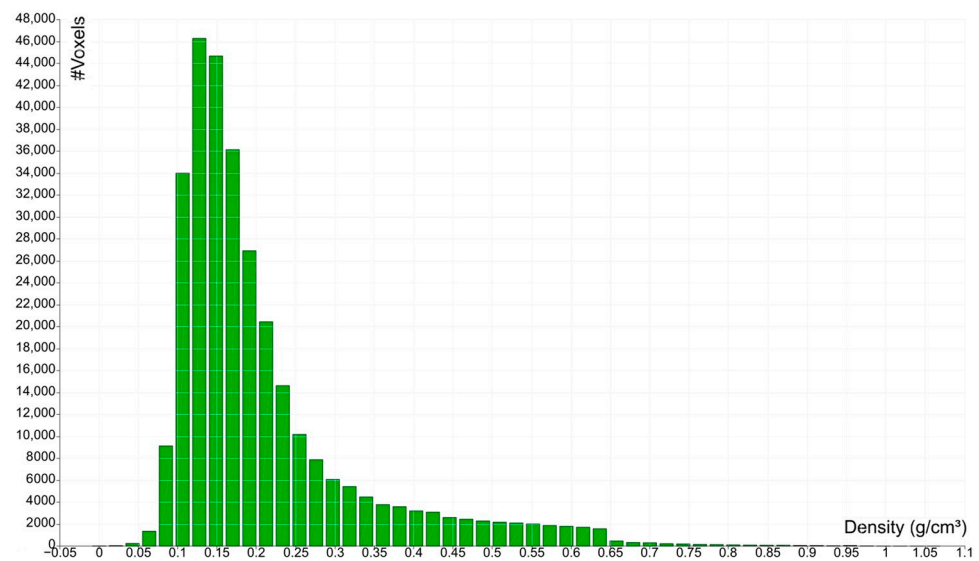

Figure 1. Density distribution in lungs ROI in g/cm^3. The distribution is characterized by a range of values from 0 to 1.06 g/cm^3, a mean value of 0.221 g/cm^3, and a median value of 0.179 g/cm^3.

This phantom will be referred to as the reference phantom throughout the manuscript, with explicit notation when variations occur (e.g., reference phantom with uniform lung density in lungs of a specified value).

Five count distribution maps (hereinafter referred to as "activity maps") were created for the reference phantom, assuming several lung shunt values (*LS* = 0%, 10%, 20%, 30%, 40%), a fixed activity concentration ratio of 5:1 for lesions with respect to the surrounding liver, and a uniform ^{90}Y activity distribution in each tissue. The total counts in the lungs were assigned using the definition of *LS* as in Equation (1)

$$LS = \frac{C_{lungs}}{C_{lungs} + C_{liver} + C_{lesions}} \tag{1}$$

where C_{lungs}, C_{liver}, and $C_{lesions}$ are the total counts in lungs, liver parenchyma, and lesions, respectively. Numerical values representing voxel activity in each tissue, i.e., lung, lesion, and liver parenchyma, were calculated with the relative calibration method [23]. This involved multiplying each voxel count by a relative calibration factor defined as the total amount of activity in the ROI over the total counts detected in that ROI, while accounting for the *LS* value.

The use of an anthropomorphic phantom aims to test the most common dosimetric approaches in RE within a framework of predefined controlled conditions that is as realistic as possible.

In this study, dosimetric evaluations obtained by classical dosimetric approaches were compared with those obtained by *MC* simulations of radiation transport in the reference phantom. The classical approaches included the mono-compartmental organ-level method

using the medical internal radiation dose (MIRD) scheme, local energy deposition (LED) at the voxel level, and convolution calculations with voxel S-values (VSV) kernels for soft and lung tissue. For the latter two methods, the specific lung voxel density (as obtained from the CT image) was incorporated into the calculations to account for lung heterogeneities as effectively as these methods allow.

2.2. Classical Approaches: Mono-Compartmental Organ Level, Local Energy Deposition, and Convolution with Soft Tissue Voxel S-Values

The mono-compartmental model of the MIRD Committee [2,3,24] (hereinafter denoted as MIRD) is a widely used approach for dosimetry at the organ level with beta-emitter radiopharmaceuticals. It enables the computation of the mean absorbed dose ($\overline{AD}$) to a specific 3D ROI, given the activity in that ROI (A_{ROI}) and the ROI's mass (M_{ROI}). The model assumes a uniform radionuclide distribution in a homogeneous medium, with all emitted radiation energy deposited within the same ROI. For ^{90}Y, using the mono-compartmental model and under the assumption (commonly used in radioembolization) of full radioactivity retention in tissues, the mean absorbed dose can be computed using the following Equation (2).

$$\overline{AD}_{ROI} = 49.38 \times \frac{A_{ROI}}{M_{ROI}} \tag{2}$$

The numerical factor in Equation (2) accounts for the physical properties of the radionuclide (i.e., the physical half-life and mean energies of the emitted β^- particle spectra as stated in the AAPM recommendations). It includes conversions between measurement units with $\overline{AD}$ expressed in Gy, activity in GBq, and mass in kg. While the mono-compartmental model is commonly used for liver dosimetry, it has also been proposed for lung dosimetry with additional approximations. For lung dosimetry, the lung mass is set to 1 kg, and the contribution to the absorbed dose in the homolateral lung of the activity in the liver dome is considered negligible [2,3]. In this study, the MIRD approach was applied according to Equation (2), using either the lungs' specific mass of the Reference phantom (724 g) or a constant mass of 1 kg.

The local energy deposition approach [23] (hereinafter referred to as LED) assumes that the energy from the decay in a given voxel is completely absorbed within the same voxel. This assumption is reasonable when the range of ^{90}Y decay electrons in tissue is comparable to voxel sizes used in nuclear medicine tomographic imaging (typically 2–5 mm). For example, in soft tissue, the mean CSDA range of the emitted electrons is approximately 5 mm. The computation is straightforward using Equation (2), referring to the activity and mass of each voxel (the latter is estimated by a calibrated CT scanner).

The convolution approach using VSV [25–27] (hereinafter referred to as SVOX) employs a 3D kernel of values that represent the absorbed dose per decay in a target voxel with its centroid positioned at (i, j, k), due to a source voxel positioned at (0, 0, 0). The VSV kernel is calculated using a dedicated *MC* simulation of electron and photon transport in a lattice of uniform medium consisting of biological tissue (e.g., soft tissue), then convoluted with the time-integrated activity distribution map to obtain the absorbed dose (AD) map. In this paper, a previously published VSV kernel for soft tissue (ST) was used [26] (methodology hereinafter referred to as SVOX_ST) to calculate the AD in the lungs as if they were composed of soft tissue. The AD was then corrected for local density variations relative to the uniform tissue density used for VSV calculations (methodology hereinafter referred to as SVOX_L), Equation (3), rescaling the voxel AD by the CT-derived lung voxel density [15]:

$$AD_{SVOX}^{Lungs}(x,y,z) = \frac{AD_{SVOX}^{ST}(x,y,z)}{\rho(x,y,z)} \times \overline{\rho}_{ST} \tag{3}$$

where $AD_{SVOX}^{ST}(x,y,z)$ is the AD to the voxel in the (x,y,z) position computed with the ST VSV kernel; $\overline{\rho}_{ST}$ is 1.04 g/cm^3 (the ST density used to compute the VSV); $\rho(x,y,z)$ is the density of the voxel in the (x,y,z) position; and $AD_{SVOX}^{Lungs}(x,y,z)$ is the AD in lungs for the

same voxel, after applying the local density correction. $\overline{AD}$ of lungs was then obtained as the mean value of the *AD* values. Given the large difference in density between ST and lungs, a lung VSV kernel was also computed in this study, assuming the International Commission on Radiation Units and Measurements (ICRU) lung tissue [21,22,28] (density of 0.296 g/cm^3) as a medium (further details are provided in the following section). Both the ST and lung VSV kernels were used to calculate the absorbed dose to the lungs for all the *LS* values, assuming uniform density or heterogeneous density and introducing corrections for the local density variations using Equation (3).

$\overline{AD}$ to lungs was calculated using classical approaches for all the activity maps defined for the Reference phantom (see Section 2.1).

2.3. Monte Carlo Simulations

All *MC* simulations of radiation transport were performed using the GATE/Geant4 code, version 8.1 [29], on a desktop computer equipped with an Intel Core i7 Extreme Edition 8 Core Processor and 16 GB of Random Access Memory (RAM). The simulations used the nested sampling algorithm for volume parametrization and the emstandart-opt3 physics model, which simulates all electromagnetic processes, including bremsstrahlung. The range cut was defined as a production threshold for secondary particles, with an R_cut of 0.1 mm. For $LS \neq 0$, 10^9 primaries were used, whereas 10^{10} primaries were used for $LS = 0\%$.

The simulation input file for the Reference phantom included activity and density map distributions in MetaImage format, a file with tissue composition information, and "macro" files with all the simulation parameters (e.g., geometry definitions, output file creations, number of primaries, decay information, etc.). The density map for the lungs was obtained through the calibration curve of the CT image, whereas the ICRU lung tissue composition [21,22] was assigned to all lung voxels based on user-defined HU ranges to identify the tissue class. Dosimetric calculations using *MC* simulations were performed for all the activity maps defined for the Reference phantom (see Section 2.1).

A dedicated *MC* simulation was also performed to calculate a new VSV kernel for the lungs, assuming the ICRU lung tissue [21,22,28] (density of 0.296 g/cm^3) as a medium. The simulation involved a uniform cube with a 600 mm side, a source voxel at its center, and 2.21 mm cubic voxels. The VSV kernel was validated by comparing the $\overline{AD}$ to lungs obtained by convolution with the value obtained by a direct *MC* simulation. For this comparison, the reference phantom had activity only in the lungs, *LS* = 10%, and a uniform lung density of 0.296 g/cm^3.

2.4. Evaluation of Mean Absorbed Doses and Relative Uncertainties

For voxel dosimetry approaches, the $\overline{AD}$ was computed in the total lungs region as follows:

$$\overline{AD} = \frac{1}{N_{Lungs}} \sum_{x,y,z} AD\,(x,y,z) \tag{4}$$

where the sum runs for all the voxels of the lung volume; N_{Lungs} is the total number of lung voxels; and $AD(x,y,z)$ is the voxel absorbed dose for the voxel in the (x,y,z) position. In this study, *AD* values, and consequently $\overline{AD}$, are always expressed as Gy per GBq of administered activity (Gy/GBq).

The relative uncertainty, Equation (5), of the $\overline{AD}$ evaluated by *MC* has been computed [30]:

$$U_{ROI,rel} = \sqrt{\frac{1}{n} \sum_{k=1}^{n} u_{k,rel}^2} \tag{5}$$

where n is the number of voxels in the ROI and $u_{k,rel}$ is the relative statistical uncertainty in the k-th voxel. The relative uncertainty maps were obtained together with the *AD* maps as output from the *MC* simulations.

The $\overline{AD}$ obtained from each dosimetric method was compared with respect to the *MC* using correlation plots, with the MC's $\overline{AD}$ on the x-axis (data obtained with the Reference phantom and the *LS* conditions) and the $\overline{AD}$ obtained from each classical approach on the y-axis. Also, relative differences, Equation (6), in $\overline{AD}$ between the tested method and *MC* were calculated.

$$RD(\%) = \frac{Tested - MC}{MC} \times 100 \qquad (6)$$

3. Results

3.1. Monte Carlo's $\overline{AD}$ Uncertainties

The $\overline{AD}$ relative uncertainty was computed using Equation (5), and the results are presented in Table 1 for each *LS* value with ranges of variation of the voxel *AD*. The $\overline{AD}$ relative uncertainty for *LS* = 0% was about 20% for 10^{10} primaries and visually represented in Figure 2 for *LS* = 40% only.

Table 1. Uncertainty (CL = 95%) of the *MC* simulation for each *LS* case. U_{ROI} corresponds to the $\overline{AD}$ uncertainty (Equation (5)), while u_{min} and u_{max} represent the minimum and maximum values of the relative uncertainty of the absorbed dose at the voxel level. An example of the *AD* distribution and relative uncertainty map is shown in Figure 2.

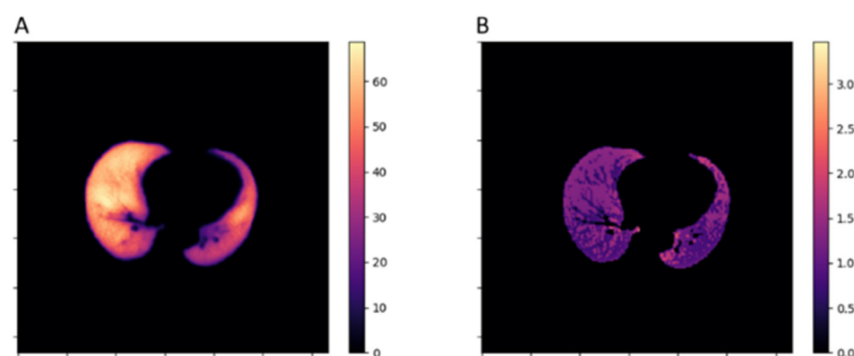| Lung Shunt	U_{ROI} (%)	u_{min}(%)	u_{max}(%)
10%	2.5	1.1	5.6
20%	1.8	0.8	3.9
30%	1.5	0.6	3.4
40%	1.3	0.6	2.7

Figure 2. *AD* distribution (values expressed in Gy/GBq) within lungs (**A**) and the associated relative uncertainty map (**B**) for *LS* = 40%.

3.2. VSV Kernel for Lung Tissue

The lung and ST VSV kernel used for convolution calculations are shown in Figure 3 as a plot of the *AD* to the target voxel per unit decay versus the target-source voxel distance. The lung VSV kernel is also provided as supplemental material for this work (S-values kernel for the lung tissue of 0.296 g/cm^3 over 2.21 mm voxel size, available in csv formatted file as position indices (*i, j, k*) followed by the absorbed dose values expressed in mGy/MBq·s). For the lung *AD* data, a long and widespread tail is observed starting at approximately 38 mm. This is due to the greater predominance of the bremsstrahlung to the *AD* for target voxels farthest from the radiation source, with an *AD* ranging from approximately $(10^{-8}$–$10^{-7})$ $\frac{mGy}{MBq \cdot s}$ (Supplementary Material). The VSV kernel for the lungs, calculated in this work, was validated by comparing the lungs' $\overline{AD}$ obtained using the SVOX method with that obtained from *MC* simulations. This comparison was performed with the reference phantom, which had activity only in the lungs, a *LS* of 10%, and a uniform lung density of 0.296 g/cm^3. Before performing SVOX calculations with the lung VSV kernel, the liver activity was cropped from the activity map. This is because the presence of

liver activity produces a cross-irradiation from the liver to the lungs that is significantly higher than that obtained by the *MC* simulation. With these assumptions, $\overline{AD}$ to lungs was 4.29 Gy/GBq with the SVOX approach, which is in good agreement with 4.23 Gy/GBq obtained from the *MC* simulation (*RD* = 1.5%). When using the SVOX calculation with the lung VSV kernel and considering only the liver activity, the cross-irradiation from the liver to the lungs was approximately 0.60 Gy/GBq. This value is considerably higher than the 0.18 Gy/GBq obtained by the *MC* simulation.
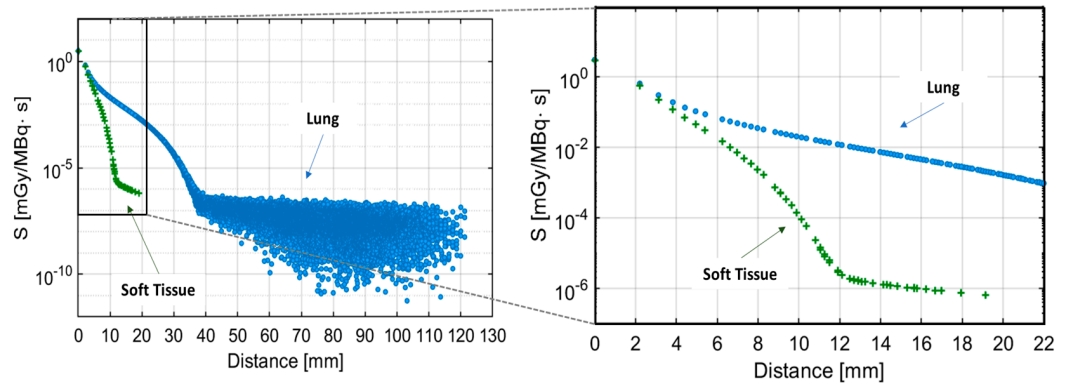

Figure 3. Plot of the *AD* per unit decay to the target voxel (y-axis) versus the source-target voxel distance (x-axis) for the previously published ST kernel (9 × 9 × 9) [26] (data freely available on the website https://www.medphys.it/down_svoxel.htm, accessed on 24 July 2024) and the lung kernel calculated in this work (32 × 32 × 32). The right plot reports the same data shown in the left plot up to a source-target of 20 mm.

3.3. Monte Carlo vs. "Classical" Approaches

Firstly, comparisons are made between the *MC* evaluations and all the "classical" approaches, i.e., the mono-compartmental MIRD approach (MIRD, using the personalized lung mass), LED, and SVOX using a previously published ST VSV kernel [26] (SVOX_ST). All results are presented in a correlation plot shown in Figure 4. This plot also includes the results obtained by rescaling the SVOX_ST data by the voxel's local density according to Equation (3) (SVOX_L).
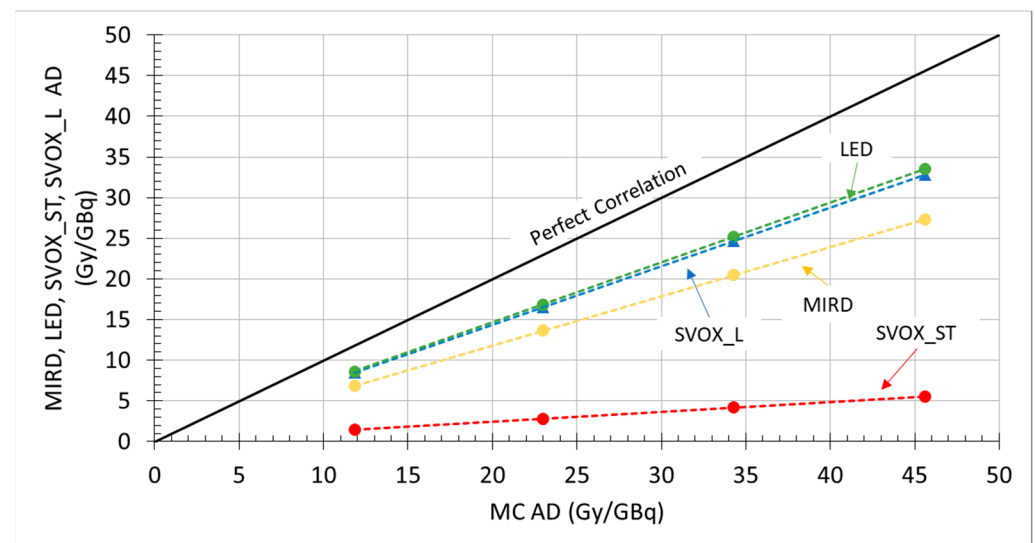

Figure 4. Correlation plot of the lungs' $\overline{AD}$, obtained from *MC* simulations with the Reference phantom (x-axis) with those from: mono-compartmental MIRD approach (MIRD), local energy deposition (LED), SVOX with ST kernel with corrections for tissue heterogeneities according to Equation (3) (SVOX_L), or without these corrections (SVOX_ST). For the SVOX_ST data, a previously

published VSV kernel for soft tissue (ST) was used [26] (data freely available on the website https://www.medphys.it/down_svoxel.htm, accessed on 24 July 2024). For each dataset, each point in the plot is associated with an increasing *LS* value (10%, 20%, 30%, and 40%), and a line representing the linear interpolation of each dataset serves as a qualitative eye guide only.

All tested methods severely underestimate the *MC* results. The RD computed according to Equation (6) is reported in Table 2, while the $\overline{AD}$ of each approach is reported in Table 3. The *RD* values are approximately −40% for MIRD, −27% for LED, −88% for SVOX_ST, and −28% for SVOX_L.

Table 2. Lungs' $\overline{AD}$ relative difference for the classical approaches with respect to the *MC* evaluations.

Lung Shunt	MIRD (%)	LED (%)	SVOX_ST (%)	SVOX_L (%)
10%	−42.4	−27.4	−87.8	−28.5
20%	−40.7	−26.7	−87.8	−28.2
30%	−40.3	−26.5	−87.8	−28.1
40%	−40.2	−26.4	−87.9	−28.1

Table 3. Lungs' $\overline{AD}$ for the *MC* simulation and the classical approaches, as visually reported in Figure 4. All the results are reported in Gy per GBq of administered activity.

Lung Shunt	MC	MIRD	LED	SVOX_ST	SVOX_L
10%	11.9	6.8	8.6	1.4	8.5
20%	23.0	13.6	16.8	2.8	16.5
30%	34.3	20.5	25.2	4.2	24.6
40%	45.6	27.3	33.6	5.5	32.8

Considering the activity map with *LS* = 0% (no activity in the lungs), all the classical approaches intrinsically yield $\overline{AD}$ = 0, whereas the *MC* simulation yields a dosimetric contribution of the radiation transport from the hepatic dome to the lungs, resulting in 0.20 Gy/GBq.

The MIRD approach using a 1 kg lung mass resulted in smaller $\overline{AD}$ to lungs (as the lung mass is 0.724 kg), with values ranging from 4.9 Gy/GBq to 19.8 Gy/GBq increasing LS, with a constant RD of −27.6% with respect to the MIRD $\overline{AD}$ obtained with personalized lung mass, due to the mass difference.

3.4. Monte Carlo vs. SVOX with the VSV Kernel for the Lung Tissue

The SVOX method, using the lung VSV kernel, was employed to calculate the *AD* to the lungs after cropping the activity map to include only the lung region. Cropping was necessary because applying the SVOX method to the entire activity map would otherwise result in anomalous dosimetric contributions from the liver (as discussed in Section 3.2). The results obtained with the new kernel (referred to as Lung_296), those globally rescaled to the mean density of the Reference phantom's lungs (referred to as Lung_221), and those locally rescaled for the tissue heterogeneities (referred to as Lung_L, according to Equation (3) and using the ICRU lung density as uniform tissue density), are shown on the y-axis of the correlation plot in Figure 5, similar to the results presented in Figure 4. For comparison, the SVOX_ST data are also included.

Even when using the new VSV kernel for lung, all the evaluations severely underestimate the results obtained from *MC* simulations. The *RD* computed according to Equation (6) and presented in Table 4 shows values around −62% for Lung_296, −50% for Lung_221, and −36% for Lung_L. The *AD* for each computational approach is reported in Table 5.
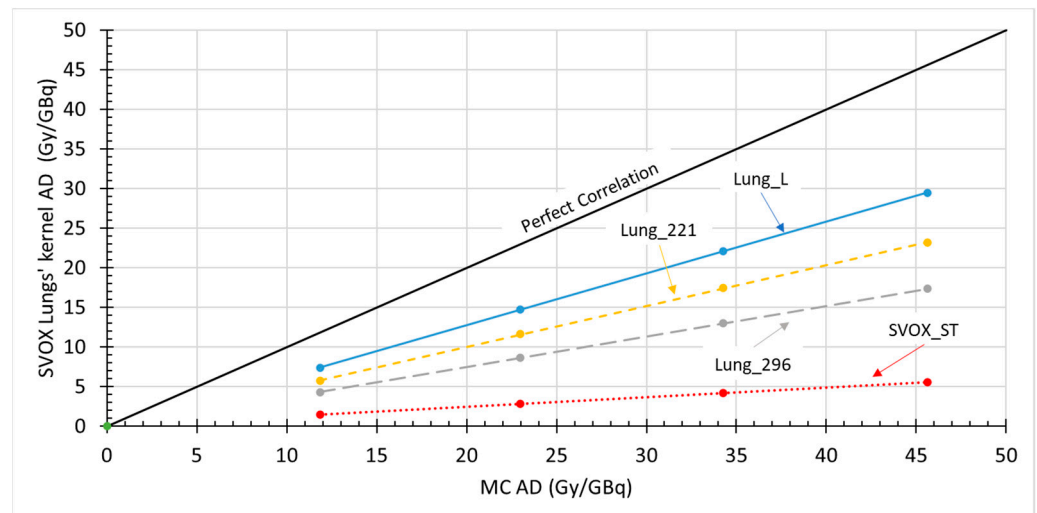
Figure 5. Correlation plot of the lungs' $\overline{AD}$, obtained from *MC* simulations with the Reference phantom (on the x-axis), compared with those obtained using the new lung VSV kernel (referred to as Lung_296), those obtained after a global correction based on the mean lung density of the Reference phantom (Lung_221), and those obtained after correcting for tissue heterogeneities according to Equation (3) (Lung_L, using 0.296 g/cm^3 as the uniform tissue density). For comparison, the SVOX_ST data (already presented in Figure 4) are also included. For each data series, each point in the plot corresponds to an increasing *LS* value (10%, 20%, 30%, and 40%), with a line representing the linear interpolation of each dataset, provided as a qualitative visual guide only.

Table 4. Relative Difference for the SVOX with the new lung tissue kernel with respect to the *MC* computed according to Equation (6).

Lung Shunt	Lung_296 (%)	Lung_221 (%)	Lung_L (%)
10%	−63.8	−51.5	−38.1
20%	−62.3	−49.5	−35.9
30%	−62.1	−49.2	−35.5
40%	−62.0	−49.1	−35.4

Table 5. Lungs' $\overline{AD}$ for the *MC* simulation and the SVOX with the new lung's VSV kernel, as visually reported in Figure 5. All the results are reported in Gy per GBq of administered activity.

Lung Shunt	MC	Lung_296	Lung_221	Lung_L
10%	11.9	4.3	5.8	7.3
20%	23.0	8.7	11.6	14.7
30%	34.3	13.0	17.4	22.1
40%	45.6	17.3	23.2	29.5

3.5. Absorbed Dose Distributions

The following section presents a visual example of the activity biodistribution simulated in this study, along with the corresponding *AD* distribution maps. Figure 6 shows the activity biodistribution for the case with an *LS* of 20% along with the corresponding *AD* distributions obtained from the *MC* simulation and several of the previously discussed convolution methods, specifically SVOX_L, Lung_296, and Lung_L. It should be noted that the *AD* distributions for Lung_296 and Lung_L do not show *AD* in the liver region. This is due to the assumption that the activity image was cropped to include only the lungs. This cropping was performed in order to prevent unrealistic contributions to *AD* in the lungs from activity in the hepatic region. The images demonstrate that the *MC AD* distribution shows higher *AD* per voxel compared to other voxel-based methods, even under more realistic physical assumptions.
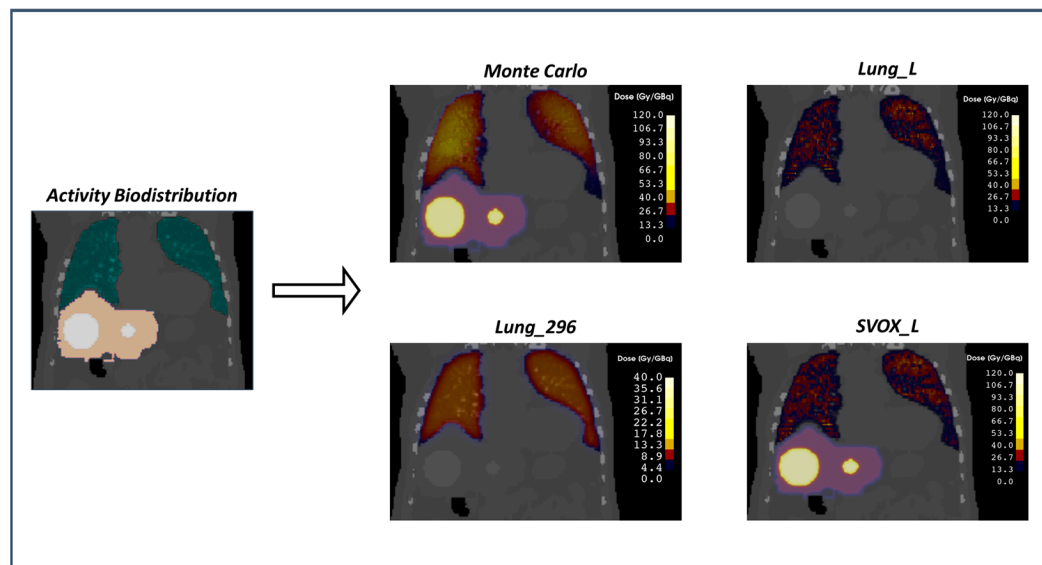
Figure 6. From left to right, this figure shows an example of the activity biodistribution for the *LS* = 20% case and the corresponding *AD* distribution maps for the *MC* simulation. Also included are the *AD* distribution maps obtained from several convolution approaches for visual comparison. The colors used to represent the activity biodistribution are purely illustrative, indicating that the activity was uniformly distributed within each region (for further details, see Section 2.1). The *AD* distributions are reported as Gy per GBq of administered activity. For Lung_296 and Lung_L, the *AD* distribution does not display any dose in the liver region, reflecting the computational choice to crop the activity map to the lung region only. Note that the *AD* distribution for Lung_296 is represented with a different color scale, from 0 to 40 Gy/GBq, compared to the other methods, which are shown with a scale from 0 to 120 Gy/GBq, because using the latter scale, the dose values would not have been visible.

3.6. Impact on Clinical Decision Making

Table 6 reports the results for the *MC* $\overline{AD}$, the activity that is as high as safely administrable (AHASA), and the maximum activity in the lungs (MLA) not to be exceeded, ensuring that the average absorbed dose to the lungs does not exceed the 30 Gy threshold [2,3] for the specific simulated case.

Table 6. *MC* $\overline{AD}$ results for all the *LS* cases and the corresponding activity that is as high as safely administrable (AHASA) and the maximum lung activity (MLA).

Lung Shunt	*MC* $\overline{AD}$ **(Gy/GBq)**	**AHASA (GBq)**	**MLA (GBq)**
10%	11.9	2.52	0.25
20%	23.0	1.30	0.26
30%	34.3	0.87	0.26
40%	45.6	0.66	0.26

It is worth noting that the safe activity in the lungs is almost the same for all *LS* values due to the negligible cross-irradiation contribution from the liver to the lungs. It is noteworthy that, for this specific patient and the simulated liver biodistribution of treatment microspheres, the maximum lung activity (MLA) is significantly lower than the typically expected MLA of approximately 600 MBq according to international guidelines [2,3]. This difference primarily arises from the physical assumptions underlying the computation of MLA using the MIRD approach. Additionally, computations using any of the other tested methods would similarly result in an overestimation of the MLA compared to the *MC* simulation.

It should be noted that all the presented results are specific to the particular morphological information of the case in this study and are not intended for general application.

None of the results should be interpreted as general criteria or as a basis for corrections to computations performed with any of the tested approaches for patients other than the one studied here. However, the overall performance of each method is indicative of its limitations, with the primary differences arising from the underlying physical assumptions of each tested approach.

4. Discussion

Using a standard desktop computer with 10^9 primaries and no variance reduction techniques, *MC* simulations on the Reference phantom took about 6 days each. The relative uncertainties affecting *AD* values (reported in Table 1) ranged from 1 to 3% for $LS \geq 10\%$. Given these benefits, the *MC* calculation method could be adapted for clinical applications with relatively minimal effort, especially when compared to the 2–3 days at most required for inverse planning in EBRT.

The validation of the presented results is supported by previously published work that internally validated the GATE code for soft tissue with controlled tissue heterogeneities. This prior research demonstrated good agreement between the *MC AD* distributions and those obtained using the MIRD and VSV method with a soft-tissue kernel [12]. Additionally, a second validation step was performed on homogeneous lung tissue with an *LS* of 20%. This step demonstrated the internal consistency of the *MC* simulation results in comparison to the VSV method using a lung tissue kernel (see Section 3.2). A more extensive validation to assess the reliability of the *MC* simulation for strongly heterogeneous lung tissue would involve comparing different *MC* codes. However, such an evaluation was beyond the scope of the present work.

Comparisons between the VSV kernels in Figure 2 highlight the specific properties of radiation transport in lung tissue compared to ST. In the lungs, the *AD* increases considerably for any given source-target distance relative to ST, as does the radiation penetration in the medium. The most abrupt slope change in the lung VSV trend occurs at approximately 38 mm. This is well-correlated with the maximum penetration of the ^{90}Y emitted beta radiation in the lung, whose maximum CSDA range is approximately 38.6 mm [31] for the β^- end-point energy of ^{90}Y; beyond that distance, the only contributions to the absorbed dose are due to bremsstrahlung radiation. Data scattering increases with the source-target distance. This is due to growing statistical uncertainty, as fewer and fewer interaction events are recorded when approaching and exceeding the maximum penetration range of beta radiation.

The use of the lung kernel on the entire patient's activity map equates to the assumption that all the patient's tissues have the same composition as the lung. For these reasons, cross-irradiation from the liver to the lungs due to the activity retained in the liver resulted in values three times higher than those obtained by *MC* simulation. Therefore, when using VSV kernels, it is crucial to apply activity map cropping for approximated *AD* calculations in scenarios where organs with highly differing densities are contiguous. This approach is particularly important for estimating the *AD* to tissues with lower densities. Some new approaches [32] have been proposed, introducing a convolution approach using mixed kernels for regions defined as soft tissue or lungs. These approaches report good agreement with reference *MC* simulations on patient data.

Comparisons of the "classical" dosimetric approaches (MIRD, LED, and VSVs with soft-tissue kernel) with reference *MC* simulations show unacceptable underestimation of the lungs' $\overline{AD}$. The MIRD and LED methodologies inherently assume a direct proportionality between the $\overline{AD}$ and the *LS*. However, the contribution of cross-irradiation from the hepatic region, as indicated by the *MC* simulations, varies depending on the activity in the liver. This results in *RD* ranging from -42% to -40% for SVOX_ST and from -26.4% to -27.4% for LED. When using the MIRD approach with a lung mass of 1 kg instead of the personalized mass, the relative differences compared to using the personalized mass are about -28%, worsening the *RD* with respect to the reference data. The largest discrepancies arise from using the SVOX methodology with the ST VSV kernel, resulting in

about −88% *RD*. This is mainly due to the higher density of the soft tissue used in the VSV calculations compared to the lung density, not counterbalanced by the increase in energy deposition, leading to lower *AD* values.

Conversely, lower differences relative to *MC* are observed with the SVOX methodology when local density corrections are applied or with the LED approach (which inherently accounts for local density variations). Notably, after applying local density corrections, the corrected SVOX data (named SVOX_L) become almost identical to the LED data. This is due to the limited penetration range of the ^{90}Y emitted radiation in ST, compared to the voxel size or spatial resolution. In this work, activity maps were modeled without imaging data, so the nominal spatial resolution is determined by the voxel size (2.21 mm). However, the abrupt decrease in the S-value means that contributions to the target voxels from distant voxels are negligible, and the main dosimetric contributions are coming from the nearest neighbors. Therefore, for ^{90}Y, using the ST VSV kernel for convolution calculations with local density corrections intrinsically approximates LED conditions.

Moreover, the initial evidence of the inaccuracy of post-convolution local density corrections is highlighted by the VSV comparison. When considerable radiation transport occurs, as expected for lung tissue, a reliable *AD* correction would require correction factors that vary with the source-target distance for each contribution to the target voxel. These issues cannot be addressed with a single correction factor based on a density ratio, as clearly demonstrated by the VSV kernel comparison. This corrective method was initially proposed for correcting voxel *AD* for slight density variations and small penetration ranges (as seen in ST). However, it has been well established that local density correction only accounts for the fluency correction of primary particles without affecting the contribution of secondary particles to the $\overline{AD}$ [15]. Therefore, this correction becomes increasingly imprecise with greater radiation penetration ranges and larger density variations in the medium.

The use of a lung VSV kernel yielded the results reported in Figure 5. The *RD* obtained using a VSV kernel specifically calculated for a lung medium density of 0.296 g/cm^3 (ICRU lung tissue [21,22,28]) varied between −63.8% and −62% compared to the reference *MC* simulation. Although the relative difference shows a slight improvement over the data obtained with the ST kernel, the agreement with the *MC* reference data remains poor. Despite the VSVs being calculated using a medium density considerably closer to the Reference phantom's mean lung density (0.221 g/cm^3), the significant discrepancy cannot be easily attributed to the density differences between the Reference phantom and the ICRU mean lung density.

A global density correction based on the average density of 0.221 g/cm^3 resulted in a still high *RD* (from −51.5% to −49.1%). Even with local density corrections, the *RD* remained unacceptable (varying from −38.1% to −35.4%).

Since the $\overline{AD}$ computed using the lung VSV kernel was in good agreement with the reference data for a homogeneous lung medium and provided activity map cropping, the observed differences should be correlated with the significant tissue heterogeneities of the lungs. If this is the case, an *MC* simulation of the reference phantom with uniform density lungs (corresponding to the mean density value of the phantom's lungs) should result in a smaller $\overline{AD}$ compared to an *MC* simulation on the same phantom with heterogeneous lung density and the same mean density. Indeed, the *RD* between the two simulations under the stated density conditions resulted in approximately −70%, clearly indicating that:

1. Radiation transport is strongly influenced by the tissue heterogeneities of the lungs, which substantially affect the absorbed dose.
2. A lung tissue with a uniform density corresponding to the average density of the case under study is not an accurate descriptor of the real tissue.

Lung density variations in this phantom range from 0 to 1.06 g/cm³, with a positively skewed distribution. A heterogeneous density pattern is generally observed in bone tissue. However, in that case, the density distribution is shifted towards a higher value, resulting in local energy deposition. This contrasts with lung tissue, for which the *MC* simulations of radiation transport are essential to achieve an accurate description of energy deposition.

The choice of this reference phantom is not representative of the entire population but is intended to address the physical nature of the problem under discussion. Density distribution varies significantly with age, individual conditions, and comorbidities [28]. Therefore, it is crucial to evaluate on a case-by-case basis the differences that arise from using different computational approaches in a realistic case. To maintain accuracy, it is essential to use a *MC* radiation transport approach tailored to the specific density distribution being treated.

Two studies [13,14] have investigated the role of lung density in the dosimetric evaluation of *LS* in radioembolization using different dosimetric approaches. Capotosti et al. [14] conducted a two-step study comparing the performance of a fast-MC Graphic Processing Unit (GPU)-driven code versus the VSV method using a soft-tissue kernel. This comparison was performed on a reference lung–liver phantom to simulate a 10% *LS* environment and was also applied to data from 24 patients. In this study, the *MC* showed an approximate RD of -60% for the VSV $\overline{AD}$ compared to the *MC* $\overline{AD}$ on the reference phantom. Additionally, the VSV method resulted in a global underestimation of the $\overline{AD}$ of lungs in the patients' dataset, which is consistent with the findings of our study. Mikell et al. [13] conducted a general analysis of lung $\overline{AD}$ for the homolateral lung using patient data. They compared *MC* simulations performed with the Electron Gamma Shower of the National Research Council of Canada (EGSnrc) against classical approaches, including LED and the VSV approach with a soft-tissue kernel. Their analysis included comparisons with and without local density corrections. In this study, the VSV approach showed a -60% *RD* with respect to MC, while the VSV approach corrected for local density and LED reported a 20% and 17% *RD*, respectively, with a global underestimation of the *MC* $\overline{AD}$ for the first method and a global overestimation of the $\overline{AD}$ for the last two. This latter result contrasts with our analysis, which showed a global overestimation of the $\overline{AD}$ for the same dosimetric approaches across all *LS* conditions in our reference phantom. This difference may be attributed to variations in patient geometry modeling in the EGSnrc simulation, such as differences in voxel density definitions and the poor image resolution of the post-therapy activity images obtained by ^{90}Y bremsstrahlung SPECT/CT.

Unlike previously published papers, this work included all commonly used dosimetric approaches for lung dosimetry in radioembolization and compared them with an *MC* simulation using a reference phantom representing the same complexity as real patients but with known lung composition and density. Additionally, our study introduces an optimized alternative method for comparison: VSV with lung tissue kernel.

Regarding the potential clinical impact of this work, Table 6 illustrates that the primary factor determining *AD* in the lungs is the activity present in the lungs themselves. For the case considered, to avoid exceeding the dose limit of 30 Gy, the lung activity should be limited to approximately 260 MBq. This translates to the maximum safely administrable activity, based on the variable *LS* considered, ranging from 2.54 to 0.65 GBq. These results highlight the unreliability of current safety limits for treatment, whether they are based on calculating the lung dose using the single-compartment MIRD model [2,3], the 20% *LS* limit [2,4], or the MLA of approximately 600 MBq [3,5]. It is also worth noting that in cases of lobar or highly selective treatments, the results presented offer considerable flexibility, potentially making it feasible to treat patients with high levels of *LS*. Nonetheless, we must acknowledge that this study does not tackle the formidable challenge of accurately predicting *LS* and the biodistribution of microspheres through pre-treatment imaging for ^{90}Y RE.

Lung dosimetry is a major issue in RE and remains a topic of ongoing debate. Increasingly, studies [33] are highlighting the need for more patient-specific approaches, emphasizing how the highly heterogeneous nature of lung can negatively impact approximated dosimetric calculation and thereby underscore the necessity for a personalized calculation approach. For instance, a recent review [34], which provides a general discussion of the state of the art regarding lung dosimetric limits in radioembolization, found that using a standard lung mass of 1 kg leads to a general overestimation of lung mass by

an average of 20%. The use of *MC* simulations for radiation transport allows to account for the patient-specific tissue description. This was demonstrated by Auditore et al. [35] in a detailed dosimetric study on a patient who exhibited a post-treatment unexpected accumulation of microspheres in a specific area of the lungs, analyzing the correlation between the inflammatory state and the absorbed dose in that particular region.

Currently, no accurate alternatives to direct *MC* simulations exist for lung dosimetry of patients undergoing radioembolization, and no guidelines have been established to assess the role and need for more accurate approaches. The latest European guidelines on radioembolization [3] clearly state that lung absorbed dose assessments must be performed using the mono-compartmental MIRD model. This model relies on available patient information, such as average lung density or the amount of activity in the lungs measured by planar or tomoscintigraphic scans. It is also noteworthy that there are no precise methodologies based on patient imaging in the clinical context to predict microsphere biodistribution in the lungs and *LS* for ^{90}Y RE, due to intrinsic differences between radiotracers (e.g., ^{99m}Tc-MAA vs. ^{90}Y microspheres). However, new deep-learning-based methodologies are currently under development to predict post-treatment microsphere distribution in the lungs [36].

The role of radioembolization in the clinical landscape is evolving beyond its initial palliative intent to become a potential curative approach [9,10,37]. This shift is exemplified by radiation segmentectomy for early-stage HCC, which has proven to be a viable alternative in specific cases where surgery or simple ablation is contraindicated or impossible. For intermediate and advanced HCC, radioembolization has demonstrated effectiveness in downstaging to resection (e.g., for central liver lesions) or transplantation. Various studies have reported better outcomes with radioembolization compared to alternative approaches, such as chemoembolization. Even patients with severe conditions such as portal vein thrombosis can undergo radioembolization as a bridge to transplantation, provided careful case selection is performed. This broad application landscape can be further expanded through personalized precision dosimetry, which enables the use of specific activity prescriptions and the delivery of high doses to the lesions. However, this introduces potential risks in managing patients with *LS*, which must be carefully addressed. Accurate personalized dosimetry based on the characteristics of the patient's specific lung tissue is crucial. Therefore, dosimetric tools such as direct *MC* simulations or dedicated VSV kernel approaches are of paramount importance.

Lung dosimetry poses unique challenges due to the extreme density heterogeneities of lung tissue and the high penetration range of beta particles in this environment. Therefore, *MC* simulation should be regarded as the gold standard for lung-based dosimetry in radioembolization. The simulation times demonstrated in this work are already compatible with clinical practice. However, increasing the availability of new *MC* codes that enable fast simulations without compromising accuracy would further support the feasibility of adopting the *MC* approach as standard practice. The concept of "fast" should not be linked to a simplified physical model (e.g., local deposition of decay electrons), but rather to hardware-wise optimization strategies, such as parallel computing on GPU cards [14,38,39], or the implementation of variance reduction techniques (VRT). While VRT can offer a straightforward and efficient means to reduce computational time, the choice of technique is constrained by the simulation code being used. Moreover, these techniques require careful testing through trial simulations to ensure that the *MC* code operates correctly both with and without VRT and to optimize the VRT parameters accordingly.

A recent study [40] also tested the feasibility of using fast semi-MC approaches based on quantitative PET images. These approaches simplify the transport simulation code by individually analyzing the interacting components in tissues and calculating the energy deposited in each voxel according to the patient's attenuation for photon interactions while assuming purely local absorption for electrons. Although faster and more realistic than a full local deposition calculation, the assumption of local electron absorption presents significant limitations, particularly for low-density, heterogeneous tissues like the lungs, as has been extensively discussed.

More advanced approaches for performing rapid calculations of absorbed dose distribution as alternatives to *MC* simulation include deep-learning-based methodologies, which are being explored for their reliability and speed. For example, convolutional neural networks can predict *AD* distributions using morphological information from CT scans and activity biodistribution from PET or SPECT scans [41,42]. Additionally, other approaches aim to predict the distribution of treatment microspheres based on pre-treatment ^{99m}Tc-MAA SPECT/CT scans, which can then be used to estimate the *AD* distribution [36].

The discussed results suggest that the *MC* approach is necessary in heterogeneous tissues of highly variable density, such as lungs. This need is already recognized in various therapeutic applications, such as radioiodine therapy for iodine-avid lung metastases from differentiated thyroid carcinoma [16] and radioimmunotherapy with ^{131}I for non-Hodgkin's lymphoma [17]. In these cases, *MC* is of paramount importance for accurately assessing tumor absorbed dose and establishing correlations between tumor regression and the average absorbed dose to healthy tissues.

5. Conclusions

Detailed lung dosimetry is crucial for safely treating patients with a non-zero lung shunt undergoing RE with ^{90}Y microspheres. Due to the high heterogeneity of lung tissue, none of the most common dosimetric approaches provide accurate lung dosimetry. This can lead to miscalculations and, in the worst-case scenario, result in unexpected radiation pneumonitis in treated patients. This study demonstrated that all classical approaches underestimate the average absorbed dose to the lungs. This discrepancy can be easily attributed to the hypotheses underlying the approximations of each computational approach, which become invalid in the presence of highly heterogeneous media.

Fortunately, internal dosimetry evaluation using *MC* simulations is now within reach for clinical applications, thanks to the reduced time needed to simulate radiation transport in lungs. The advent of dedicated GPU-based Monte Carlo codes could enhance our ability to describe and accurately measure *AD* distributions and reduce computational time significantly. This advancement could pave the way for a more personalized and optimized approach to treatment planning in radioembolization.

References

1. Bray, F.; Ferlay, J.; Soerjomataram, I.; Siegel, R.L.; Torre, L.A.; Jemal, A. Global cancer statistics 2018: GLOBOCAN estimates of incidence and mortality worldwide for 36 cancers in 185 countries. *CA Cancer J. Clin.* **2018**, *68*, 394–424. [CrossRef] [PubMed]
2. Dezarn, W.A.; Cessna, J.T.; DeWerd, L.A.; Feng, W.; Gates, V.L.; Halama, J.; Kennedy, A.S.; Nag, S.; Sarfaraz, M.; Sehgal, V.; et al. Recommendations of the American Association of Physicists in Medicine on dosimetry, imaging, and quality assurance

procedures for 90Y microsphere brachytherapy in the treatment of hepatic malignancies. *Med. Phys.* **2011**, *38*, 4824–4845. [CrossRef] [PubMed]

3. Weber, M.; Lam, M.; Chiesa, C.; Konijnenberg, M.; Cremonesi, M.; Flamen, P.; Herrmann, K. EANM procedure guideline for the treatment of liver cancer and liver metastases with intra-arterial radioactive compounds. *Eur. J. Nucl. Med. Mol. Imaging* **2022**, *49*, 1682–1699. [CrossRef] [PubMed]

4. Sirtex: SIR-Spheres® Microspheres. Available online: https://www.sirtex.com/ap/products/sir-spheres-y-90-resin-microspheres/about-sir-spheres/approved-indication/ (accessed on 13 August 2024).

5. BTG: TheraSphere® Yttrium-90 Glass Microspheres. Available online: https://www.nrc.gov/docs/ML1427/ML14279A535.pdf (accessed on 13 August 2024).

6. Levillain, H.; Bagni, O.; Deroose, C.M.; Dieudonné, A.; Gnesin, S.; Grosser, O.S.; Flamen, P. International recommendations for personalised selective internal radiation therapy of primary and metastatic liver diseases with yttrium-90 resin microspheres. *Eur. J. Nucl. Med. Mol. Imaging* **2021**, *48*, 1570–1584. [CrossRef]

7. Salem, R.; Padia, S.A.; Lam, M.; Chiesa, C.; Haste, P.; Sangro, B.; Garin, E. Clinical, dosimetric, and reporting considerations for Y-90 glass microspheres in hepatocellular carcinoma: Updated 2022 recommendations from an international multidisciplinary working group. *Eur. J. Nucl. Med. Mol. Imaging* **2023**, *50*, 328–343. [CrossRef] [PubMed]

8. Roosen, J.; Klaassen, N.J.; Westlund Gotby, L.E.; Overduin, C.G.; Verheij, M.; Konijnenberg, M.W.; Nijsen, J.F.W. To 1000 Gy and back again: A systematic review on dose-response evaluation in selective internal radiation therapy for primary and secondary liver cancer. *Eur. J. Nucl. Med. Mol. Imaging* **2021**, *48*, 3776–3790. [CrossRef]

9. Ahmed, A.; Stauffer, J.A.; LeGout, J.D.; Burns, J.; Croome, K.; Paz-Fumagalli, R.; Toskich, B. The use of neoadjuvant lobar radioembolization prior to major hepatic resection for malignancy results in a low rate of post hepatectomy liver failure. *J. Gastrointest. Oncol.* **2021**, *12*, 751–761. [CrossRef]

10. Tohme, S.; Sukato, D.; Chen, H.W.; Amesur, N.; Zajko, A.B.; Humar, A.; Tsung, A. Yttrium-90 radioembolization as a bridge to liver transplantation: A single-institution experience. *J. Vasc. Interv. Radiol.* **2013**, *24*, 1632–1638. [CrossRef]

11. Kim, H.C.; Kim, G.M. Radiation pneumonitis following Yttrium-90 radioembolization: A Korean multicenter study. *Front. Oncol.* **2023**, *13*, 977160. [CrossRef]

12. Milano, A.; Gil, A.V.; Fabrizi, E.; Cremonesi, M.; Veronese, I.; Gallo, S.; Pacilio, M. In Silico Validation of MCID Platform for Monte Carlo-Based Voxel Dosimetry Applied to 90Y-Radioembolization of Liver Malignancies. *Appl. Sci.* **2021**, *11*, 1939. [CrossRef]

13. Mikell, J.K.; Mahvash, A.; Siman, W.; Mourtada, F.; Kappadath, S.C. Comparing voxel-based absorbed dosimetry methods in tumors, liver, lung, and at the liver-lung interface for (90)Y microsphere selective internal radiation therapy. *Eur. J. Nucl. Med. Mol. Imaging Phys.* **2015**, *2*, 16. [CrossRef]

14. Capotosti, A.; Moretti, R.; Vaccaro, M.; Ribeiro, C.D.A.; Placidi, L.; Nardini, M.; Meffe, G.; Cusumano, D.; Zagaria, L.; De Risi, M.; et al. The Role of Lung Density in the Voxel-Based Dosimetry of 90Y-TARE Evaluated with the Voxel S-Value (VSV) Method and Fast Monte Carlo Simulation. *Appl. Sci.* **2024**, *14*, 1019. [CrossRef]

15. Dieudonné, A.; Hobbs, R.F.; Lebtahi, R.; Maurel, F.; Baechler, S.; Wahl, R.L.; Gardin, I. Study of the impact of tissue density heterogeneities on 3-dimensional abdominal dosimetry: Comparison between dose kernel convolution and direct Monte Carlo methods. *J. Nucl. Med.* **2013**, *54*, 236–243. [CrossRef] [PubMed]

16. Song, H.; He, B.; Prideaux, A.; Du, Y.; Frey, E.; Kasecamp, W.; Sgouros, G. Lung dosimetry for radioiodine treatment planning in the case of diffuse lung metastases. *J. Nucl. Med.* **2006**, *47*, 1985–1994.

17. Dewaraja, Y.K.; Wilderman, S.J.; Ljungberg, M.; Koral, K.F.; Zasadny, K.; Kaminiski, M.S. Accurate dosimetry in 131I radionuclide therapy using patient-specific, 3-dimensional methods for SPECT reconstruction and absorbed dose calculation. *J. Nucl. Med.* **2005**, *46*, 840–849.

18. Yushkevich, P.A.; Piven, J.; Hazlett, H.C.; Smith, R.G.; Ho, S.; Gee, J.C.; Gerig, G. User-guided 3D active contour segmentation of anatomical structures: Significantly improved efficiency and reliability. *Neuroimage* **2006**, *31*, 1116–1128. [CrossRef] [PubMed]

19. Fedorov, A.; Beichel, R.; Kalpathy-Cramer, J.; Finet, J.; Fillion-Robin, J.C.; Pujol, S.; Kikinis, R. 3D Slicer as an image computing platform for the Quantitative Imaging Network. *Magn. Reason. Imaging* **2012**, *30*, 1323–1341. [CrossRef] [PubMed]

20. Meijering, E.H.W.; Niessen, W.J.; Pluim, J.P.; Viergever, M.A. Quantitative Comparison of Sinc-Approximating Kernels for Medical Image Interpolation. International Conference on Medical Image Computing and Computer-Assisted Intervention. In Proceedings of the Medical Image Computing and Computer-Assisted Intervention–MICCAI'99: Second International Conference, Cambridge, UK, 19–22 September 1999.

21. ICRU. *Tissue Substitutes in Radiation Dosimetry and Measurement*; ICRU Report No 44; International Commission on Radiation Units and Measurements: Bethesda, MD, USA, 1989; Volume 23.

22. ICRU. *Photon, Electron, Proton, and Neutron Interaction Data for Bodytissues*; ICRU Report No 46; International Commission on Radiation Units and Measurements: Bethesda, MD, USA, 1992; Volume 24.

23. Chiesa, C.; Sjogreen-Gleisner, K.; Walrand, S.; Strigari, L.; Flux, G.; Gear, J.; Konijnenberg, M. EANM dosimetry committee series on standard operational procedures: A unified methodology for ^{99m}Tc-MAA pre- and ^{90}Y peri-therapy dosimetry in liver radioembolization with ^{90}Y microspheres. *Eur. J. Nucl. Med. Mol. Imaging Phys.* **2021**, *8*, 77. [CrossRef] [PubMed]

24. Bolch, W.E.; Eckerman, K.F.; Sgouros, G.; Thomas, S.R. MIRD Pamphlet No. 21: A Generalized Schema for Radiopharmaceutical Dosimetry—Standardization of Nomenclature. *J. Nucl. Med.* **2009**, *50*, 477–484. [CrossRef]

25. Bolch, W.E.; Bouchet, L.G.; Robertson, J.S.; Wessels, B.W.; Siegel, J.A.; Howell, R.W.; MIRD Committee. MIRD pamphlet No. 17: The dosimetry of nonuniform activity distributions--radionuclide S values at the voxel level. Medical Internal Radiation Dose Committee. *J. Nucl. Med.* **1999**, *40*, 11S–36S.

26. Lanconelli, N.; Pacilio, M.; Meo, S.L.; Botta, F.; Di Dia, A.; Aroche, L.T.; Cremonesi, M. A free database of radionuclide voxel S values for the dosimetry of nonuniform activity distributions. *Phys. Med. Biol.* **2012**, *57*, 517–533. [CrossRef]

27. Pacilio, M.; Amato, E.; Lanconelli, N.; Basile, C.; Torres, L.A.; Botta, F.; Cremonesi, M. Differences in 3D dose distributions due to calculation method of voxel S-values and the influence of image blurring in SPECT. *Phys. Med. Biol.* **2015**, *60*, 1945–1964. [CrossRef] [PubMed]

28. Van Dyk, J.; Keane, T.J.; Rider, W.D. Lung density as measured by computerized tomography: Implications for radiotherapy. *Int. J. Radiat. Oncol. Biol. Phys.* **1982**, *8*, s1363–s1372. [CrossRef]

29. Jan, S.; Santin, G.; Strul, D.; Staelens, S.; Assié, K.; Autret, D.; Morel, C. GATE: A simulation toolkit for PET and SPECT. *Phys. Med. Biol.* **2004**, *49*, 4561. [CrossRef] [PubMed]

30. Chetty, I.J.; Rosu, M.; Kessler, M.L.; Fraass, B.A.; Ten Haken, R.K.; McShan, D.L. Reporting and analyzing statistical uncertainties in Monte Carlo-based treatment planning. *Int. J. Radiat. Oncol. Biol. Phys.* **2006**, *65*, 1249–1259. [CrossRef]

31. Berger, M.; Coursey, J.; Zucker, M. ESTAR, PSTAR, and ASTAR: Computer Programs for Calculating Stopping-Power and Range Tables for Electrons, Protons, and Helium Ions (Version 1.21). 1999. Available online: http://physics.nist.gov/Star (accessed on 13 August 2024).

32. Chen, G.; Lu, Z.; Jiang, H.; Lin, K.H.; Mok, G.S. Voxel-S-Value based 3D treatment planning methods for Y-90 microspheres radioembolization based on Tc-99m-macroaggregated albumin SPECT/CT. *Sci. Rep.* **2023**, *13*, 4020. [CrossRef] [PubMed]

33. Dodson, C.R.; Marshall, C.; Durieux, J.C.; Wojtylak, P.F.; Davidson, J.C.; Muzic, R.F.; Kardan, A. Using an Assumed Lung Mass Inaccurately Estimates the Lung Absorbed Dose in Patients Undergoing Hepatic [90]Yttrium Radioembolization Therapy. *CardioVascular Interv. Radiol.* **2022**, *45*, 1793–1800. [CrossRef]

34. Kappadath, S.C.; Lopez, B.P.; Salem, R.; Lam, M.G.E.H. Reassessment of the lung dose limits for radioembolization. *Nucl. Med. Commun.* **2021**, *42*, 1064–1075. [CrossRef]

35. Auditore, L.; Amato, E.; Boughdad, S.; Meyer, M.; Testart, N.; Cicone, F.; Gnesin, S. Monte Carlo ^{90}Y PET/CT dosimetry of unexpected focal radiation-induced lung damage after hepatic radioembolisation. *Phys. Med. Biol.* **2020**, *65*, 235014. [CrossRef]

36. Plachouris, D.; Tzolas, I.; Gatos, I.; Papadimitroulas, P.; Spyridonidis, T.; Apostolopoulos, D.; Kagadis, G.C. A deep-learning-based prediction model for the biodistribution of ^{90}Y microspheres in liver radioembolization. *Med. Phys.* **2021**, *48*, 7427–7438. [CrossRef]

37. Yu, Q.; Khanjyan, M.; Fidelman, N.; Pillai, A. Contemporary applications of Y90 for the treatment of hepatocellular carcinoma. *Hepatol. Commun.* **2023**, *7*, e0288. [CrossRef] [PubMed]

38. Schiavi, A.; Senzacqua, M.; Pioli, S.; Mairani, A.; Magro, G.; Molinelli, S.; Patera, V. Fred: A GPU-accelerated fast-Monte Carlo code for rapid treatment plan recalculation in ion beam therapy. *Phys. Med. Biol.* **2017**, *62*, 7482–7504. [CrossRef] [PubMed]

39. Lemaréchal, Y.; Bert, J.; Falconnet, C.; Després, P.; Valeri, A.; Schick, U.; Visvikis, D. GGEMS-Brachy: GPU GEant4-based Monte Carlo simulation for brachytherapy applications. *Phys. Med. Biol.* **2015**, *60*, 4987–5006. [CrossRef] [PubMed]

40. Zeimpekis, K.G.; Mercolli, L.; Conti, M.; Sari, H.; Rominger, A.; Rathke, H. [90]Y post-radioembolization clinical assessment with whole-body Biograph Vision Quadra PET/CT: Image quality, tumor, liver and lung dosimetry. *Eur. J. Nucl. Med. Mol. Imaging* **2024**, *51*, 2100–2113. [CrossRef]

41. Lee, M.S.; Hwang, D.; Kim, J.H.; Lee, J.S. Deep-dose: A voxel dose estimation method using deep convolutional neural network for personalized internal dosimetry. *Sci. Rep.* **2019**, *9*, 10308. [CrossRef]

42. Li, Z.; Fessler, J.A.; Mikell, J.K.; Wilderman, S.J.; Dewaraja, Y.K. DblurDoseNet: A deep residual learning network for voxel radionuclide dosimetry compensating for single-photon emission computerized tomography imaging resolution. *Med. Phys.* **2022**, *49*, 1216–1230. [CrossRef]